

COMPUTATIONAL INVESTIGATION OF COAXIAL ROTOR AERODYNAMICS IN HOVER

Vinod K Lakshminarayan *
Alfred Gessow Rotorcraft Center
Department of Aerospace Engineering
University of Maryland
College Park, MD 20742

Karthikeyan Duraisamy †
Rotor Aeromechanics Lab
Department of Aerospace Engineering
University of Glasgow
Glasgow G12 8QQ
United Kingdom

James D. Baeder ‡
Alfred Gessow Rotorcraft Center
Department of Aerospace Engineering
University of Maryland
College Park, MD 20742

Abstract

In this work, a compressible Reynolds Averaged Navier Stokes (RANS) solver is used to investigate the aerodynamics of a coaxial rotor configuration under hovering conditions. The objective of this work is to evaluate the predictive capability of the computational approach and to characterize the unsteadiness in the aerodynamic flow-field of a coaxial system. Additionally, the effect of rotor spacing on the unsteadiness is studied. To assess the accuracy of the baseline methodology, single rotor simulations are compared with experiments. On gaining sufficient confidence in the approach, extensive validation studies are performed on a two-bladed coaxial rotor system. Although detailed yaw-trimming is not achieved, global quantities such as thrust and power are predicted to within 5% accuracy. The interaction between the rotor systems is seen to generate significant impulses in the instantaneous thrust and power. The characteristic signature of this impulse is explained in terms of the blade thickness (a *venturi effect*) and loading (an *upwash-downwash* effect). As expected, increased rotor spacing is seen to reduce both the thickness and loading effects. Further, interaction of the top-rotor wake with the blades of the bottom rotor results in low-harmonic unsteadiness.

Introduction

Conceptually, the coaxial rotor configuration offers substantial design advantages over the conventional main rotor tail-rotor configuration. Perhaps most significantly, the additional power requirements and weight associated with the tail rotor, tail boom and transmission system may be reallocated for additional payload capability. Additionally, the asymmetry of lift associated with a single rotor in forward flight is mitigated, offering the potential for a faster and more stable vehicle. Reductions in size and noise are also advantages often cited for the conceptual coaxial configuration.

However, in a coaxial rotor configuration, the two ro-

tors and their wakes interact with each other, producing a more complicated flow field than is found in a single rotor system. A major portion of the lower rotor continually operates in the wake system of the upper rotor. This has a significant effect on the inflow distribution of the overall system, and also on the boundary layer of the lower rotor blades. This interacting flow can, in general, result in a loss of net rotor system aerodynamic efficiency. Additionally, this can result in an undesired unsteadiness in the flow field even under hovering conditions.

Coleman (Ref. 1) presents a concise summary of coaxial rotor experiments along with a comprehensive list of relevant citations on performance, wake characteristics,

* Graduate Research Assistant, vinodkl@umd.edu

† Lecturer, dkarthik@eng.gla.ac.uk

‡ Associate Professor, baeder@eng.umd.edu

and proposed methods of performance analysis. Traditionally, for multiple rotor systems, simple analyses such as blade element momentum theory (Refs. 2, 3) or vortex filament methods (VFM) (Refs. 2, 4–8) have been used. These methods can provide for a qualitative understanding of the phenomena and predict global performance characteristics within reasonable accuracy. Recently, the Vorticity Transport Model (VTM) (Ref. 9) has been applied to the coaxial rotor system. In this approach, the wake vorticity is determined from a lifting line-based approach and is evolved in the flow-field using an Eulerian solution of the inviscid, incompressible vorticity transport equations. The representation of the wake is of a much higher quality, and as a result, more accurate performance predictions are reported. Though the aforementioned methods are efficient and are capable of producing accurate results, the following limitations have been observed:

- A certain degree of empiricism is involved. For instance, in VFM, initial core-radius and vortex roll-up are required.
- These models are inviscid, and therefore, the drag information is required and the vortex/wake decay is either ignored or modeled.
- Since the blade is represented as a lifting line, the surface information is lost, and hence effects due to the blade thickness and vortex-surface interaction cannot be captured.

The goal of this work is to use a compressible Reynolds Averaged Navier–Stokes (RANS) solver to study the performance and flow physics of a coaxial rotor. In this approach, the solution of a higher level approximation of the fluid flow equations coupled with an accurate representation of the blade geometry can be expected to provide further insight into the aerodynamics and performance of the coaxial system. It has to be recognized however, that a different set of challenges are involved in such a simulation and these have to be sufficiently addressed before the solver can be used in a design environment.

A major difficulty in RANS-based CFD simulations of the coaxial rotor computations is the enormous computational cost required to handle the counter-rotating system. Additionally, the effect of the wake is highly significant since one is interested in its interaction with the rotor blades. Therefore, it becomes imperative to resolve the vortex development and represent the vortex structure over possibly, hundreds of chord lengths of evolution. Hence, accurate numerical schemes and reliable turbulence models need to be used and the resulting methodology needs to be carefully validated with experiments if the CFD results are to be considered reliable. Recently,

Duraisamy & Baeder (Refs. 10, 11) used the high order accurate overset RANS code, OVERTURNS, to simulate the single bladed hovering rotor experiment of Martin et al (Ref. 12). For the first time, detailed validations of the swirl and axial velocities were achieved up to one full revolution of the wake (roughly 60 chords of evolution). In addition, the aerodynamic loading was validated on single rotor systems. The present work seeks to extend the application of the methodology to a coaxial rotor system. As a first step, high resolution computations are performed on a hovering coaxial rotor and validated with experimental results. An analysis of the aerodynamics is also presented.

Methodology

The computations are performed using the compressible RANS solver OVERTURNS (Ref. 10). To allow for adequate mesh resolution and ease of grid generation, structured overset meshes are used. Time integration is performed using the second order implicit Backwards Difference method scheme with Lower-Upper Symmetric Gauss-Siedel (LUSGS) method (Ref. 13) for inversion. In hovering single rotor calculations, it is typical to solve the Navier-Stokes equations in the rotating reference frame (Ref. 14) such that a steady solution is sought. However, the inherently unsteady nature of the flow field in the current work requires the use of time-accurate calculations. Therefore, in this paper, all the computations (including the single rotor calculations) are performed in a time-accurate manner in the inertial frame of reference. The LUSGS inversion is used along with Newton sub-iterations (Ref. 15) to remove factorization errors and to recover time accuracy. The chosen time-steps correspond to 0.25° and 0.125° of azimuth for the coarse and fine mesh computations, respectively. The inviscid spatial terms are computed using a third order MUSCL scheme with Roe's flux difference splitting and the viscous terms are computed using second order central differencing. The Spalart-Allmaras (Ref. 16) turbulence model is employed for the RANS closure. This one-equation model has the advantages of ease of implementation, computational efficiency and numerical stability. The production term in this eddy-viscosity model is modified (Ref. 10) to account for the reduction of turbulence in the vortex core due to flow rotation effects. The downwash velocity in the bottom plane of the rotor can be significant. In order to account for this and to properly represent the inflow at the other far-field boundaries, the point-sink boundary condition approach of Srinivasan et al. (Ref. 14) is used for both single and coaxial rotor systems.

Single Rotor Validation

This section describes the computations performed on various two-bladed experimental setups. The measurements of McAlister et al. (Ref. 17) and Harrington (Ref. 18) were chosen to demonstrate the capability of OVERTURNS to predict the overall performance and the setup of Caradonna and Tung (Ref. 19) is used to validate surface pressure distributions. A two mesh overset system with a body-conforming blade mesh and a cylindrical background mesh are used for all the cases. The periodicity of the flow-field is utilized and hence, only half the computational domain is simulated.

McAlister rotor [Thrust/Power prediction]

The experimental setup consists of a two-bladed rigid rotor with an aspect ratio of 6. The profile of the blade is a NACA0020 airfoil at 0.2R that linearly tapers to a NACA0012 at 0.5R. The profile remains a NACA0012 from 0.5R to 1.0R. The blade is set at a collective of 8° . Validation is done for the case with Reynolds number of 1.6×10^6 and the tip Mach number of 0.387. The blade mesh has $267 \times 155 \times 111$ points in the streamwise, spanwise and normal directions, respectively and the background cylindrical mesh has $127 \times 186 \times 198$ points in the azimuthal, radial and vertical directions, respectively (see Fig. 1). The experimental value of C_T and C_Q are reported as 0.00500 and 0.000500, respectively. The predicted values of C_T and C_Q are 0.00480 and 0.000512, respectively. The comparison shows that OVERTURNS gives a reasonable performance prediction for a single two-bladed rigid rotor configuration.

Harrington rotor [Performance prediction]

Harrington conducted experiments on two different rotors in both single and coaxial rotor configurations. The experimental data (referred to as Rotor-2) is used to validate both single and coaxial rotor systems. The experimental setup consists of a two-bladed rigid rotor with an aspect ratio of 8.33. The blade uses a NACA airfoil with a linearly varying thickness of 27.5% at 0.2R to 15% at R. The tip Reynolds number is 3.5×10^6 and the tip Mach number is 0.352. Different collective pitch settings from 4° to 12° were used to obtain the variation of thrust with power. The blade mesh has $267 \times 78 \times 56$ points in the streamwise, spanwise and normal directions, respectively and the background cylindrical mesh has $97 \times 135 \times 118$ points in the azimuthal, radial and vertical directions, respectively.

Figure 2 shows the computed performance along with the experimental results. The results are reasonably good with a slight over-prediction of power at lower collec-

tive pitch settings and minor under-prediction of power at higher collectives for a given thrust. As a result, the figure of merit is slightly underpredicted at lower collectives and marginally over-predicted at higher collectives.

Caradonna rotor [Surface pressure prediction]

The experimental setup consists of a two-bladed rigid rotor in a hover chamber. The blades have a rectangular planform and are untwisted with a radius of 1.143m. The aspect ratio of the blade is 6. The blades use a NACA0012 airfoil section along the entire span. A precone angle of 0.5° was set for the blades. Validations were done for the case with blade collective of 8° . The tip Reynolds number is 1.96×10^6 and the tip Mach number is 0.439. The blade mesh has $267 \times 155 \times 111$ points in the streamwise, spanwise and normal directions, respectively and the background cylindrical mesh has $127 \times 186 \times 198$ points in the azimuthal, radial and vertical directions, respectively.

Figure 3 shows the blade pressures at various spanwise locations. It is seen that the computations agree well with the measured distributions.

Coaxial Rotor Validation

Hovering coaxial rotor simulations can be simplified if cylindrical background meshes are used. The periodicity of the flow-field can be utilized by incorporating the sliding mesh interface condition between the two rotor systems, allowing complete simulation using just one blade mesh in each rotor system. Figure 4 shows a schematic of the blade surface and the blade and background mesh boundaries. The solid lines show the meshes for the simulated blade and the dotted lines depict periodicity. The sliding boundary condition for the simulated background mesh of any of the two rotors is implemented by exchanging information with either the simulated background mesh or the periodic mesh of the other rotor. This type of interface condition, though novel in helicopter calculations, is routinely used in simulations of gas turbine rotor-stator flow-fields.

As mentioned earlier, the coaxial experimental setup of Harrington Rotor-2 (Ref. 18) is used to validate the computational predictions. It consists of two 2-bladed rotors arranged to form a coaxial system. The rotors are similar to the one used in single rotor setup. The solidity of each of the rotors is 0.076 with rotor spacing, $H/D = 0.08$ (1.33 chords).

A four mesh system consisting of two blade meshes and two cylindrical background meshes was used. The blade mesh and the background mesh of each rotor form

an overset system. The background meshes communicate with each other by means of a sliding mesh interface as explained earlier. The computations are performed on two different mesh systems as shown in Table 1. Mesh system 1 is obtained by leaving out every other point in the spanwise and normal directions from mesh system 2. Mesh system 1 is used to validate the performance and mesh system 2 is used to assess grid independence and also for flow visualization. Computations on mesh system 2 are performed only for selected collective pitch settings.

Figure 5 shows the blade and cylindrical meshes for mesh system 2. The blade mesh of the top rotor is sufficiently fine in the tip region to resolve the tip vortex formation. For the bottom rotor, the grid is redistributed such that the inboard region is highly refined in order to resolve the wake interaction. In the most refined regions, the background mesh has a grid spacing of 0.02 chords and 0.033 chords, respectively in the radial and the vertical directions. Along the azimuthal direction, a grid plane is spaced every 2° . The outer boundary of the background mesh extends to 1.5R above the top rotor, 3R below the bottom rotor and 1.5R from the tip of the blade.

Performance Comparison

In the experimental test, the top and bottom rotors were torque balanced by selecting the appropriate collective pitch. In lieu of the cost of each trim cycle using CFD, collective settings provided by Ananthan (Ref. 2) are used for the present computations. The settings obtained using the vortex filament method for various target values of thrust are provided in Table 2. Tables 3 and 4 respectively summarize the mean values of thrust (C_T) and power (C_Q) coefficients obtained from CFD for individual rotors as well as for the entire system. Table 4 also shows the difference between the top and bottom rotor mean power. It can be seen that the total mean thrust from the computation is close to the target value of the lower order model especially at higher collectives. However, the mean power coefficients of the top and bottom rotors do not match exactly and therefore, the coaxial rotor system is not yaw-trimmed. The order of difference between the rotor powers is around 10% – 12% of the total power. The reason for this is the inconsistency between the CFD and vortex filament methods. The question then, arises as to whether this data can indeed be compared with the measurements. From Harrington's experiment, it is seen that small deviations from the trim state produce similar total torque as a trimmed system for the same total thrust. This is considered acceptable at this point to compare the total forces obtained from the present CFD calculation with the yaw-trimmed experimental data for validation purposes.

Tables 3 and 4 also show the thrust and power coefficient obtained using the fine mesh for cases 2 and 7. The integrated quantities obtained using the fine mesh are not significantly different from that of the coarse mesh and hence, it is reasonable to consider the coarse mesh results for validation of performance data.

A measure of the unsteadiness in thrust and power is the root mean square value of the temporal variations and this is summarized in Tables 5 and 6. As a general trend, the absolute value of the fluctuation increases with increasing collective pitch settings, however, the relative fluctuation with respect to the mean value is seen to decrease. Additionally, when the fluctuations of the whole system is compared to that of the individual rotors, it is seen that though the absolute value is higher, the relative fluctuation is smaller. Further details of the temporal variation will be presented later in this section.

Figure 6(a) compares the computed variation of mean total thrust coefficient with mean total power coefficient with the measured values. The total performance is well predicted. At lower collectives, the power is slightly over-predicted for a given thrust, whereas at higher collectives, the power is marginally under-predicted for a given thrust level. The values from the fine mesh computation are seen to agree with the trend. It should be noted that the results from the free-vortex method (Ref. 2) also showed good agreement with the experiment. Figure 6(b) shows the mean performances of individual rotors (zero collective case is excluded). It is interesting to note that the performance of the top rotor is very similar to that of a single rotor. However, for the bottom rotor, the performance degrades because of the influence of the wake from the top rotor.

Figure 7 shows the temporal variation of C_T and C_Q over one revolution for case 7. Note that, when viewed from above, the top rotor rotates in an anti-clockwise fashion and the bottom rotor rotates clockwise. Therefore, the azimuthal locations of the top and bottom rotors are measured in their respective directions of rotation. From the figure, the unsteadiness is clearly seen with a dominant 4/rev frequency (number of times a blade of one rotor encounters a blade of the other rotor in one revolution). A higher frequency variation can be seen in the form of spikes when the blades are very close to each other. Such a variation can be attributed to the venturi effect caused by the thickness of the blades, which leads to a reduction in pressure between the rotors. As a result, the thrust of the top rotor spikes down whereas the thrust of the bottom rotor spikes up. Apart from the venturi effect, there is also an upwash-downwash effect created by the bound circulation of the blades. These effects are schematized in Fig. 8. As the blades of the top and bottom rotors approach each other, each of the blades induce an upwash on the other blade. The upwash increases as

the blades approach each other, but after a certain point it starts decreasing, changes sign and acts as a downwash. The strength of the downwash is seen to initially increase and then starts decreasing as the blades move away from each other. Correspondingly, the forces on both the top and the bottom rotor increase as the blades approach, then decrease and then increase again as they move away. Furthermore, while the thrust and the power of the top rotor show an impulsive but phased behavior, for the bottom rotor which lies in the wake of the top rotor, the features are more spread out and distinct.

Figure 9 shows the temporal variation of thrust and power for the zero collective case. From the figure, it can be seen that, at all times, the top and bottom rotors produce almost equal and opposite thrust resulting in a net zero thrust, while the power of both rotors are almost identical. This behavior is expected, because for this zero collective case, the loading and wake effects are negligible and only the venturi effect is prominent. Therefore, for both top and bottom rotors, the forces remain constant for most of the time, being impulsive only when the blades pass each other.

The loading and wake effects can be isolated from the thickness effect for a thrust producing case, to first order, by subtracting the values of the zero collective case from the thrust obtained at a given collective setting. Figure 10 shows the temporal variation of C_T and C_Q in one revolution for case 7, after subtracting the values from case 1. Also shown are the unmodified values. The spikes are clearly seen to be reduced when examining the modified forces, confirming that the venturi effect is one of the main causes for the impulsive behavior and can be considered, to first order, to not depend on the rotor collectives. The remaining impulsiveness is due to the contribution from the upwash-downwash effect. Additionally, the effect of the tip vortex interaction with the bottom rotor blade can be clearly seen in the modified thrust variation, when the value becomes almost constant with time.

Figure 11 shows the temporal variation of C_T and C_Q over one revolution for cases 2-9. As the collective pitch is decreased, the peak of the bottom rotor forces, which is expected to occur when the tip vortex from the top rotor interacts with the bottom rotor, moves to a later azimuth. This is a result of the decreased inflow leading to a slower vertical convection of the tip vortex.

Figure 12(a) shows the spanwise lift distribution for both the top and the bottom rotors at azimuthal locations of 0° and 45° for case 7. At 0° azimuth, due to the venturi effect discussed earlier, the top rotor has a lower lift, whereas the bottom rotor has a higher lift compared to the values at 45° azimuth. Additionally, a dip is noticeable in the lift coefficient of the bottom rotor at 0° azimuth. This is due to the interaction of the tip vortex from the top rotor with the bottom rotor (as will be evident from the flow

visualization results). The relative location of the dip suggests that the wake of the top rotor has contracted to $0.75R - 0.8R$. Figure 12(b) compares the spanwise lift distribution of the top rotor with a single rotor system at the same collective as the top rotor. As expected, the spanwise distribution at the 45° azimuth for the top rotor is closer to that of a single rotor compared to that at 0° azimuth. The thrust on the top rotor is slightly lower than that on the isolated rotor due to the slight increase in the downwash from the bottom rotor. Besides, the tip vortex from the single rotor does not convect down as much as the tip vortex from the top rotor of the coaxial system due to a smaller inflow. As a result, the returning tip vortex will have a larger influence on the spanwise lift distribution of a single rotor as compared to that of the top rotor of the coaxial system. Figure 13 shows the average top and bottom rotor lift distributions along with the RMS values of the temporal fluctuation along the span for both the coarse and fine meshes. While the predicted average top rotor lift distribution is very similar for both the coarse and fine meshes, the distribution for the bottom rotor is slightly different. This is because the fine mesh resolves the wake interaction better. The predicted values of the RMS fluctuation are similar for both the coarse and fine mesh cases.

An azimuthal contour of the sectional lift ($c_l M^2$) and its fluctuation from the mean value are respectively plotted in Figs. 14 and 15, for both the top and bottom rotors. The figures clearly show the large fluctuations in the outer portions of the rotors as they pass by each other, as well as the additional unsteadiness on the bottom rotor as the wake from the top rotor encounters the plane of the bottom rotor.

Effect of Rotor Spacing

In order to analyze the effect of rotor spacing, case 7 was run for two other hypothetical rotor spacings, with one and half times (2 chords) and twice (2.66 chords) the original separation. Figure 16 shows the temporal variation of the top and bottom rotor thrust and power over one revolution for all three cases. As the rotor spacing increases, both the thickness and loading effects decrease. Therefore, smaller spikes are observed with increasing separation. The mean values of the integrated quantities do not vary significantly, except for the bottom rotor power, which marginally decreases with increasing spacing. The mean value of total thrust for the three cases (in ascending order of separation distances), is respectively 0.00703, 0.00716 and 0.00721 and the mean total power is 0.000721, 0.000687 and 0.000685. Additionally, due to a decreased intensity of interaction between the two rotors, the amplitude of the variation decreases for both the top and bottom rotors. The RMS value of total thrust

variation for the three cases are 0.000443, 0.000275 and 0.000185 and the RMS value of total power variation is 0.0000394, 0.0000150 and 0.0000097.

The effect of rotor spacing can be better quantified by investigating the frequency content in the integrated quantities. In Fig. 17, the amplitude of the discrete frequency components of the various quantities are normalized by the amplitude of its own 4/rev frequency, whereas in Fig. 18, the amplitude of the frequency is normalized by the amplitude of the 4/rev frequency of the baseline case. It is seen that in all the cases (except the top rotor power), 4/rev is the dominant frequency. For the top rotor power, the dominant frequency is 12/rev for the baseline case and 8/rev for increased rotor spacing. The presence of these higher frequencies is due to the sharper nature of the impulses. Therefore, as expected, an increase in the rotor spacing decreases the high frequency content. This could be significant from the view point of acoustic noise propagation. Additionally, it is also evident that the relative amplitude of various frequencies decrease as the rotor spacing increases. It should also be noted that the bottom rotor has lesser high frequency content relative to the dominant 4/rev frequency.

Flow-field Visualization

Figure 19 shows the vorticity magnitude contours for case 7 at different azimuthal locations in space. The zero azimuth corresponds to the instant when the top and bottom rotors are perfectly aligned with each other. As the azimuth increases, the wake-age of the top rotor vortex increases, whereas that of the bottom rotor vortex decreases. Hence, it is seen that as the azimuth increases, the vortex trailed from the top rotor moves downwards, while the vortex trailed from the bottom rotor moves upwards. At all azimuths, the top and bottom rotor tip vortices can be clearly distinguished. The vortex trailed from the top rotor has contracted more and is seen to pass very close to the bottom rotor blade at 0° azimuth. Additionally, as expected, the tip vortex of the top rotor convects at a faster rate compared to that of the bottom rotor. At later wake ages, the tip vortices from the top and bottom rotor blades are seen to interact, resulting in a very complicated flow-field.

In order to extract only the rotational flow regions and not the highly strained regions, the so-called q-criterion (Ref. 20) is shown in Fig. 20(a). The tip vortices are resolved for 2 blade passages. Beyond this wake-age, the background mesh becomes too coarse to accurately represent the details of the tip vortex. After passing the bottom rotor, there is a significant interaction between the tip vortices. Figure 20(b) shows the tip vortex from the top rotor passing close to the bottom rotor. It is clearly seen that even after the interaction, the tip vortex from the top

rotor remains coherent.

Conclusions

A compressible Reynolds Averaged Navier Stokes (RANS) solver was applied to simulate the aerodynamics of single and coaxial rotor configurations in hover. The computations were performed on structured body-conforming blade meshes, overset in a cylindrical background mesh. The computations were validated with experimentally measured mean thrust and power and the sources of unsteadiness were examined. The quantitative and qualitative effects of varying the rotor spacing was investigated. The following are specific conclusions that can be drawn from the present work :

- The validation studies for a single rotor system show good agreement with the experimental performance and pressure distribution data.
- The overall performance is predicted reasonably well for the coaxial system. The performance of the top rotor was similar to that of a single rotor, but the bottom rotor showed a degradation of performance due to the influence of the top rotor wake.
- The computed performance data showed that the flow-field of a coaxial rotor is unsteady with a dominant 4/rev frequency. As a result of the finite thickness of the blade surfaces, the integrated thrust and power showed an impulsive behavior when the blades of the top and bottom rotor were aligned. Additional impulsiveness is generated due to the blade loading.
- The thrust and power of the top rotor showed an impulsive but phased behavior, whereas for the bottom rotor the features are more spread out and distinct.
- An increased rotor spacing was seen to reduce the amplitude and bandwidth of the frequency response of the thrust and power.
- The tip vortices from both the top and bottom rotor blades were preserved until two blade passages. It was observed that the tip vortex from the top rotor passes very close to the bottom rotor blade. This interaction, along with that between tip vortices from the top and bottom rotors, produce a highly complicated flow field.

Future Work

The primary focus of the present work was on the prediction of hover performance of a coaxial system using

CFD. As a continuing work, the authors plan to pursue an in-depth study of the flow physics. Computations will be performed on a finer mesh, such that there is sufficient refinement even in the inboard region to capture the vortex sheet and its interaction with other sheets accurately. A complete trimming procedure will be implemented to perform torque-trimmed computations. Finally, the effects of the fuselage will be included. Once the hovering condition is properly simulated, CFD computations can be performed in forward flight.

Acknowledgments

The authors would like to thank Dr. Shreyas Ananthan (Ref. 2) and Mr. Hyowon Kim (Ref. 9) for providing the trim collective settings of the Harrington's coaxial rotor setups.

References

- ¹Coleman, C. P., "A Survey of Theoretical and Experimental Coaxial Rotor Aerodynamic Research," Proceedings of the 19th European Rotorcraft Forum, Como, Italy, September 14–16, 1993.
- ²Leishman, J. G., and Ananthan, S., "Aerodynamic Optimization of a Coaxial Proprotor," *62nd Annual Forum of the American Helicopter Society*, 2006.
- ³Leishman, J. G., "Principles of Helicopter Aerodynamics," Cambridge University Press, 2002.
- ⁴Leishman, J. G., Bhagwat, M. J., and Bagai, A., "Free- Vortex Filament Methods for the Analysis of Helicopter Rotor Wakes," *Journal of Aircraft*, Vol. 39, (5), September-October, 2002, pp. 759-775.
- ⁵Andrew, M. J., "Coaxial Rotor Aerodynamics," Ph.D. Thesis, Southampton University, England. c. 1981.
- ⁶Bagai, A. and Leishman, J. G., "Free-Wake Analysis of Tandem, Tilt-Rotor and Coaxial Rotor Configurations," *Proceedings of the 51st Annual Forum of the American Helicopter Society*, 1995.
- ⁷Griffiths, D. A., Leishman, J. G., "A Study of Dual-Rotor Interference and Ground Effect Using a Free-Vortex Wake Model," *Proceedings of the 58th Annual Forum and Technology Display of the American Helicopter Society International*, 2002.
- ⁸Nagashima, T. and Nakanishi, K., "Optimum Performance and Wake Geometry of a Coaxial Rotor in Hover," *Vertica*, vol. 7, pp. 225-239, 1983.
- ⁹Kim, H. W., and Brown, R. E., "Coaxial Rotor Performance and Wake Dynamics in Steady and Manoeuvring flight," *Proceedings of the 62nd Annual Forum and Technology Display of the American Helicopter Society International*, 2006.
- ¹⁰Duraisamy, K., "Studies in Tip Vortex Formation, Evolution and Control," *PhD Thesis, Department of Aerospace Engineering, University of Maryland at College Park*, 2005.
- ¹¹Duraisamy, K., Sitaraman, J. and Baeder, J., "High Resolution Wake Capturing Methodology for Accurate Simulation of Rotor Aerodynamics," *61st Annual Forum of the American Helicopter Society*, 2005.
- ¹²Martin, P. B., Pugliese, G. J., and Leishman, J. G., "High Resolution Vortex Measurements in the Wake of a Hovering Rotor," *57th Annual Forum of the American Helicopter Society Proceedings*, Phoenix, AZ, 2001.
- ¹³Yoon, S. and Jameson, A., "Lower-Upper Symmetric-Gauss-Seidel Method for the Euler and Navier-stokes Equations," *AIAA Journal*, Vol. 26, 1988.
- ¹⁴Srinivasan, G. R., and Baeder, J. D., "TURNS: A Free-wake Euler/ Navier-Stokes Numerical method for Helicopter Rotors," *AIAA Journal*, Vol. 31, No. 5, 1993.
- ¹⁵Pulliam, T., "Time Accuracy and the use of Implicit Methods," *AIAA Paper 1993-3360*, 1993.
- ¹⁶Spalart, P. R. and Allmaras, S. R., "A One Equation Turbulence Model for Aerodynamics Flow," *AIAA Paper 92-0439*, 1992, pp. 1–22.
- ¹⁷McAlister, K. W., Schuler, C. A., Branum, L. and Wu J. C., "3-D Wake Measurements Near a Hovering Rotor for Determining Profile and Induced Drag," *NASA Technical paper 3577*, 1995.
- ¹⁸Harrington, R. D., "Full-Scale Tunnel Investigation of the Static Thrust Performance of a Coaxial Helicopter Rotor," *NACA Technical note 2220*, 1950.
- ¹⁹Caradonna, F.X. and Tung, C., "Experimental and Analytical Studies of a Model Helicopter Rotor in Hover," *NASA TM 81232*, 1981.
- ²⁰Jeong, J. and Hussain, F., "On the Identification of a Vortex," *J. Fluid. Mech.*, 285, 1995, pp. 69–94.

mesh	blade mesh (top and bottom)	background mesh (top)	background mesh (bottom)	Total points
1	$267 \times 78 \times 56$	$97 \times 135 \times 31$	$97 \times 135 \times 90$	3.9M
2	$267 \times 155 \times 111$	$97 \times 270 \times 61$	$97 \times 270 \times 180$	15.7M

Table 1: Sizes of different meshes used for coaxial computation.

Case	C_T (Target)	θ_0 (top rotor)	θ_0 (bottom rotor)
1	0.000	0.00°	0.00°
2	0.002	3.86°	4.42°
3	0.003	4.87°	5.47°
4	0.004	5.73°	6.33°
5	0.005	6.50°	7.08°
6	0.006	7.20°	7.75°
7	0.007	7.85°	8.43°
8	0.008	8.62°	9.14°
9	—	9.25°	9.75°

Table 2: Collective settings for the top and bottom rotors of the coaxial system.

Case	C_T (top rotor)	C_T (bottom rotor)	C_T (total)
1	-0.00052	0.00055	0.00003
2	0.00124	0.00130	0.00253
2*	0.00108	0.00121	0.00228
3	0.00182	0.00179	0.00361
4	0.00241	0.00216	0.00457
5	0.00287	0.00252	0.00539
6	0.00336	0.00283	0.00619
7	0.00378	0.00326	0.00703
7*	0.00374	0.00296	0.00670
8	0.00430	0.00366	0.00796
9	0.00459	0.00413	0.00872

Table 3: Computed mean C_T .(* indicates fine mesh)

Case	C_Q (top rotor)	C_Q (bottom rotor)	C_Q (total)	$ C_{Q_{top}} - C_{Q_{bot}} $
1	0.000121	0.000124	0.000245	0.000003
2	0.000157	0.000190	0.000347	0.000033
2*	0.000154	0.000177	0.000331	0.000023
3	0.000190	0.000226	0.000416	0.000036
4	0.000226	0.000263	0.000489	0.000037
5	0.000261	0.000300	0.000560	0.000039
6	0.000297	0.000338	0.000635	0.000041
7	0.000334	0.000387	0.000721	0.000053
7*	0.000338	0.000356	0.000694	0.000018
8	0.000383	0.000441	0.000824	0.000058
9	0.000421	0.000505	0.000925	0.000084

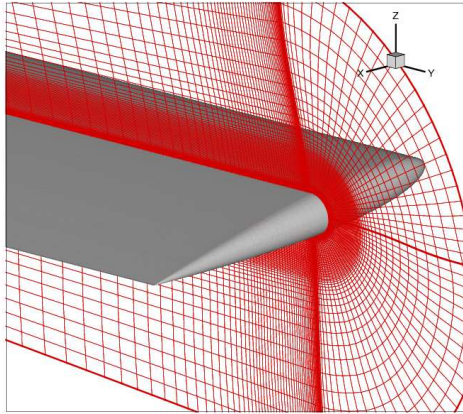
Table 4: Computed mean C_Q .(* indicates fine mesh)

Case	$dC_{T_{rms}}$ (top rotor)	% fluctuation	$dC_{T_{rms}}$ (bottom rotor)	% fluctuation	$dC_{T_{rms}}$ (total)	% fluctuation
1	0.000191	36.50%	0.000194	35.40%	0.000023	91.26%
2	0.000241	19.43%	0.000164	12.61%	0.000185	7.31%
2*	0.000240	22.22%	0.000163	13.47%	0.000211	9.25%
3	0.000269	14.78%	0.000178	9.94%	0.000268	7.42%
4	0.000285	11.83%	0.000192	8.88%	0.000336	7.35%
5	0.000304	10.59%	0.000224	8.88%	0.000397	7.36%
6	0.000318	9.46%	0.000247	8.73%	0.000427	6.90%
7	0.000341	9.02%	0.000242	7.42%	0.000443	6.30%
7*	0.000336	8.98%	0.000264	8.92%	0.000465	6.94%
8	0.000359	8.35%	0.000262	7.16%	0.000476	5.98%
9	0.000398	8.67%	0.000267	6.46%	0.000511	5.86%

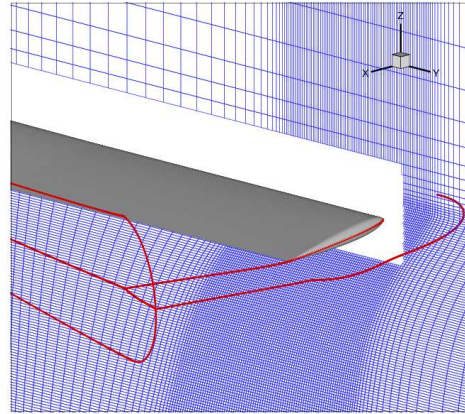
Table 5: Computed RMS fluctuation of C_T .(* indicates fine mesh)

Case	$dC_{Q_{rms}}$ (top rotor)	% fluctuation	$dC_{Q_{rms}}$ (bottom rotor)	% fluctuation	$dC_{Q_{rms}}$ (total)	% fluctuation
1	0.0000145	11.92%	0.0000150	12.11%	0.0000295	12.01%
2	0.0000149	9.49%	0.0000182	9.58%	0.0000292	8.41%
2*	0.0000133	8.64%	0.0000189	10.68%	0.0000281	8.49%
3	0.0000171	9.00%	0.0000193	8.54%	0.0000297	7.14%
4	0.0000196	8.67%	0.0000205	7.79%	0.0000315	6.44%
5	0.0000219	8.39%	0.0000227	7.57%	0.0000350	6.25%
6	0.0000245	8.25%	0.0000247	7.31%	0.0000383	6.03%
7	0.0000282	8.44%	0.0000241	6.23%	0.0000394	5.46%
7*	0.0000251	7.43%	0.0000217	6.10%	0.0000348	5.01%
8	0.0000323	8.43%	0.0000257	5.83%	0.0000432	5.24%
9	0.0000390	9.26%	0.0000284	5.62%	0.0000505	5.46%

Table 6: Computed RMS fluctuation of C_Q .(* indicates fine mesh)



(a) Blade meshes



(b) Cylindrical meshes with blade mesh boundaries

Figure 1: Computational mesh for McAlister rotor.

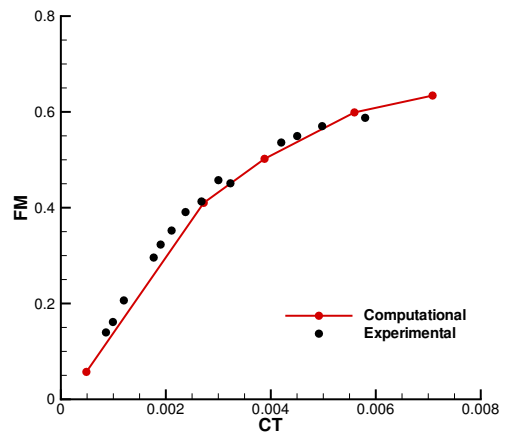
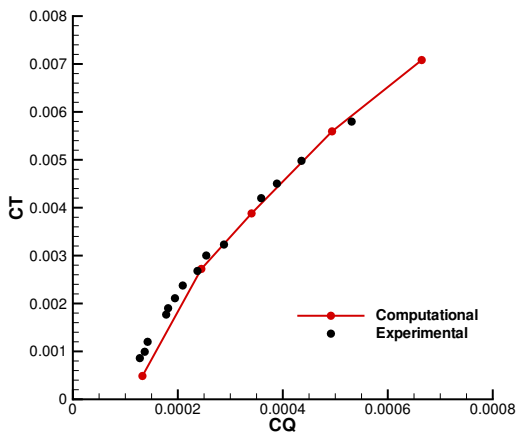
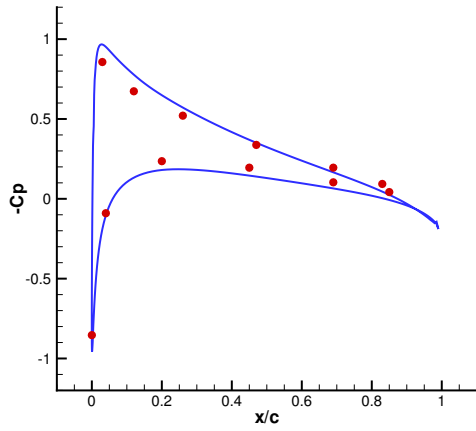
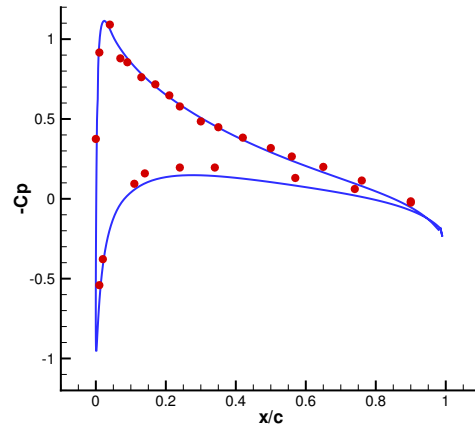


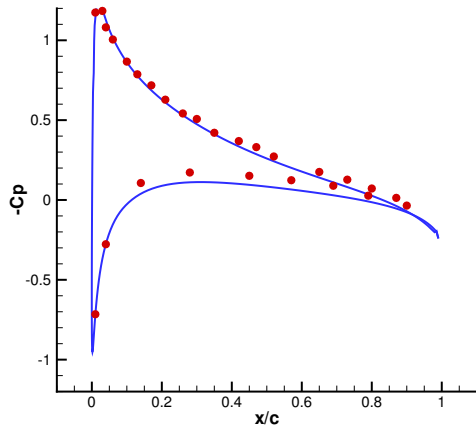
Figure 2: Computed and experimental performance for Harrington single rotor.



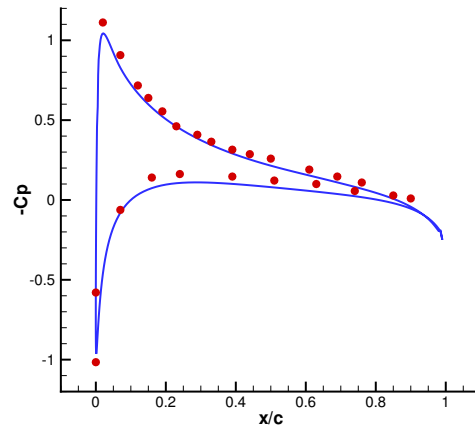
(a) $r/R=0.50$



(b) $r/R=0.80$



(c) $r/R=0.89$



(d) $r/R=0.96$

Figure 3: Comparison of computed blade surface pressure (lines) coefficient with experiment (circles) for Caradonna Rotor.

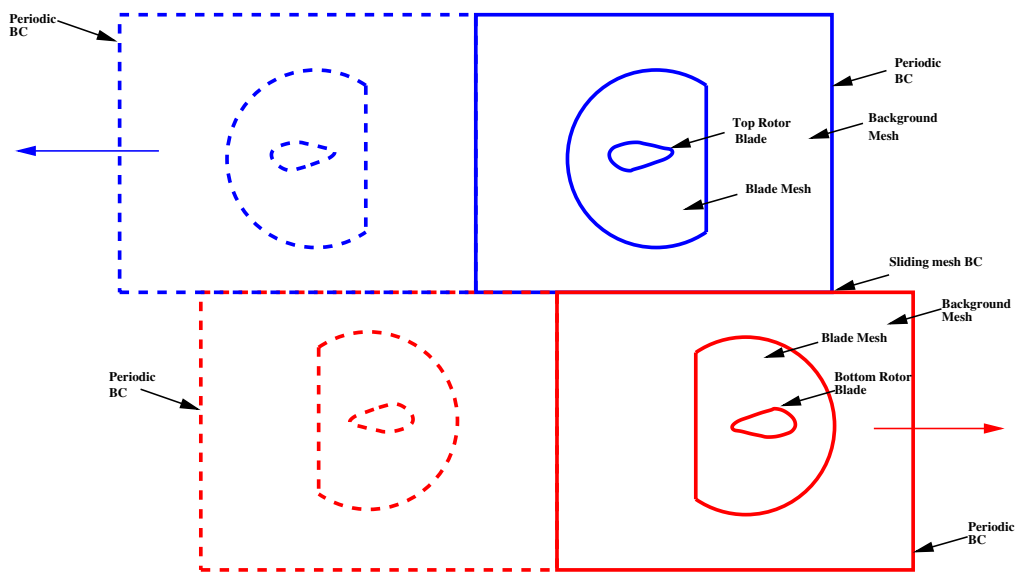


Figure 4: Schematic of the mesh system and the boundary condition for a 2-bladed coaxial rotor.

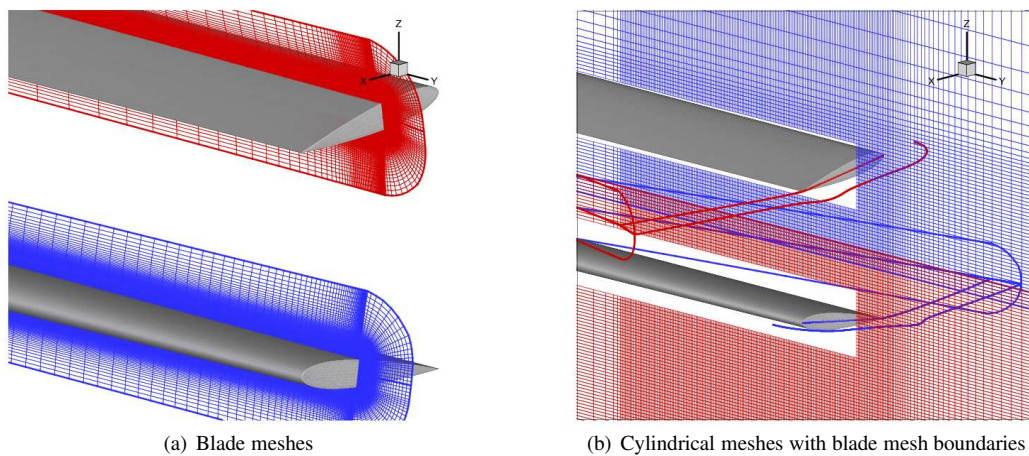
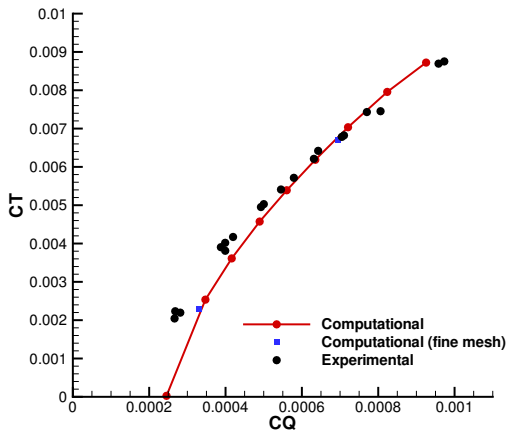
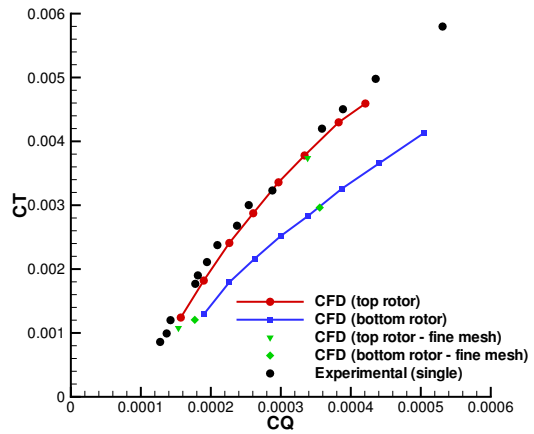


Figure 5: Computational mesh (mesh system 2) for the coaxial rotor system.

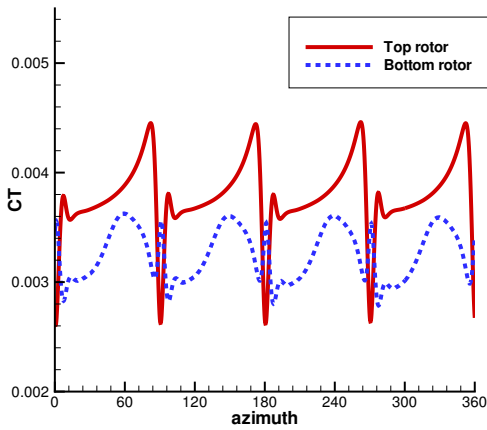


(a) Total C_T (mean) versus total C_Q (mean)

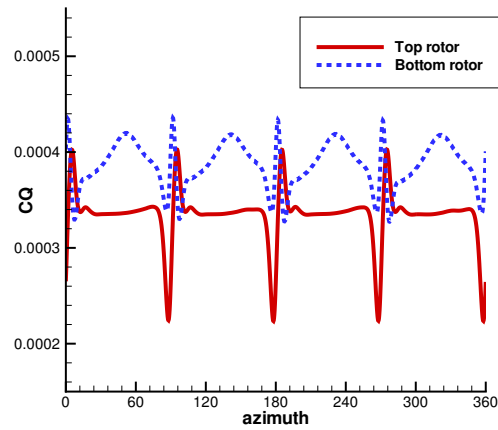


(b) C_T (mean) versus C_Q (mean) for individual rotors.

Figure 6: Comparison of performance for the coaxial rotor.



(a) C_T variation



(b) C_Q variation

Figure 7: Temporal variation of C_T and C_Q of the top and bottom rotors over the last revolution for the coaxial system (case 7).

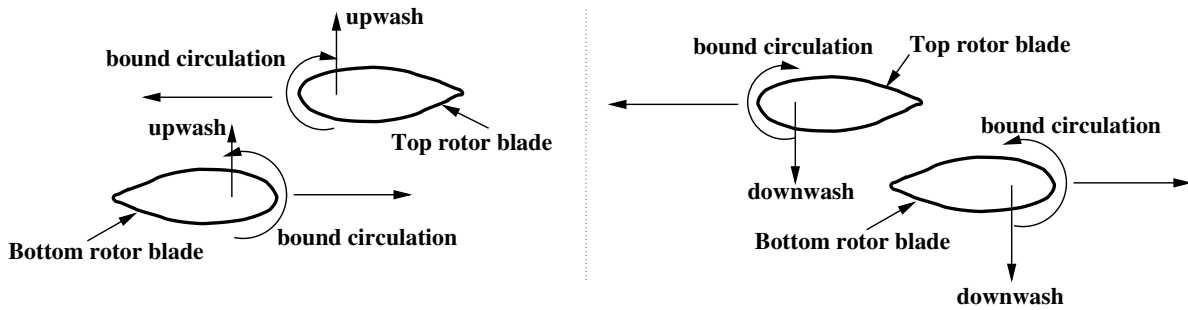
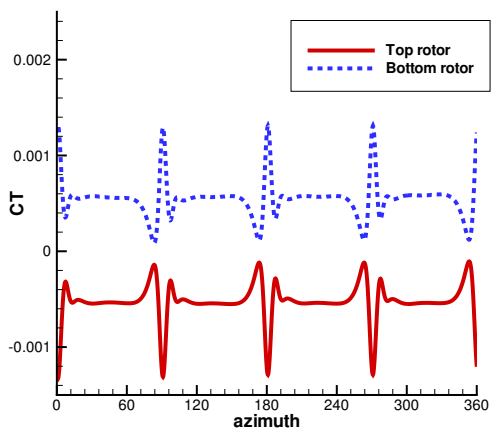
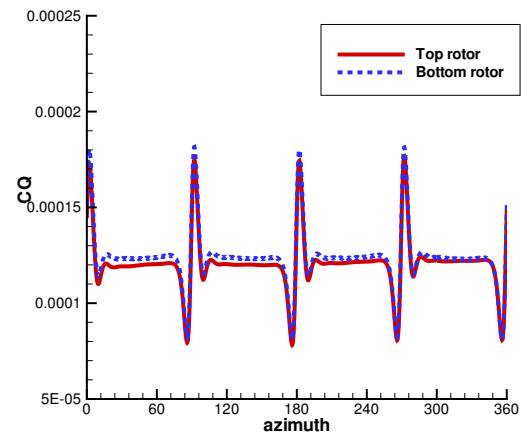


Figure 8: Schematic of the loading (upwash-downwash) effect.

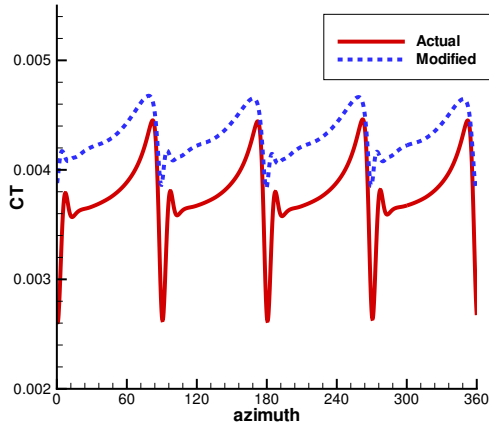


(a) C_T variation

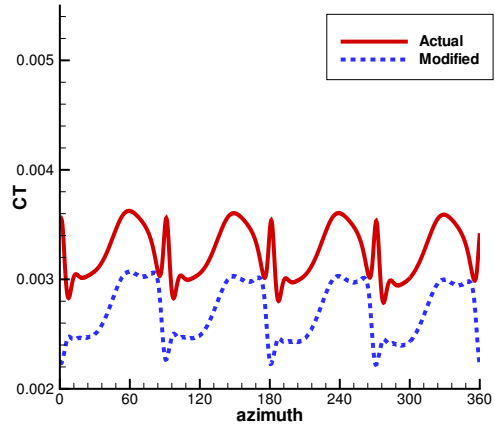


(b) C_Q variation

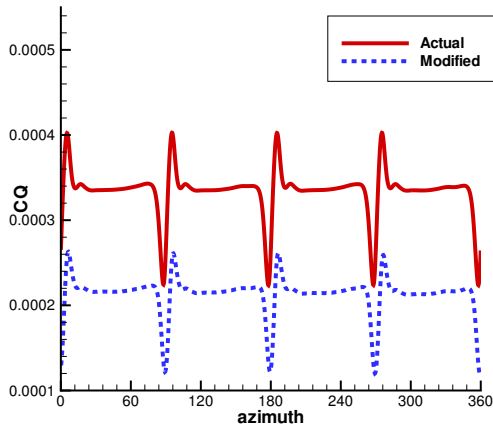
Figure 9: Temporal variation of C_T and C_Q of the top and bottom rotors in the last revolution for the coaxial system (case 1).



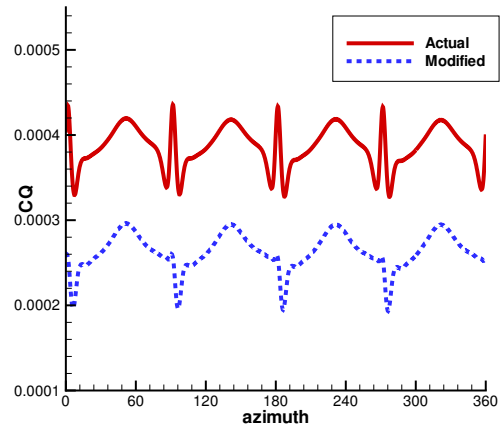
(a) Top rotor C_T variation



(b) Bottom rotor C_T variation

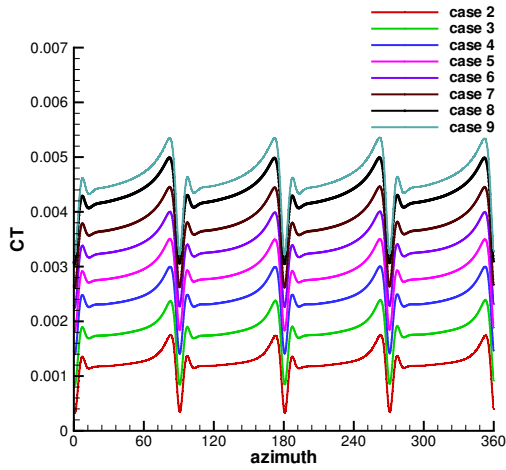


(c) Top rotor C_Q variation

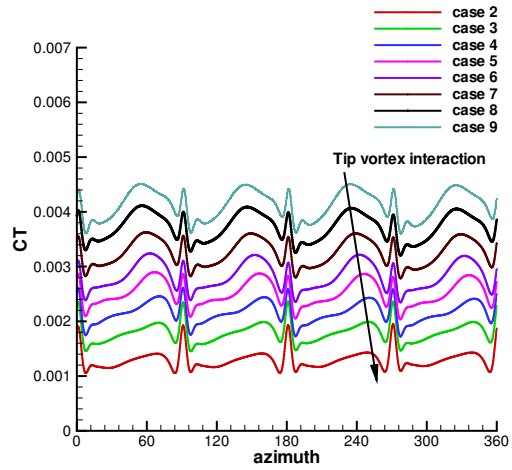


(d) Bottom rotor C_Q variation

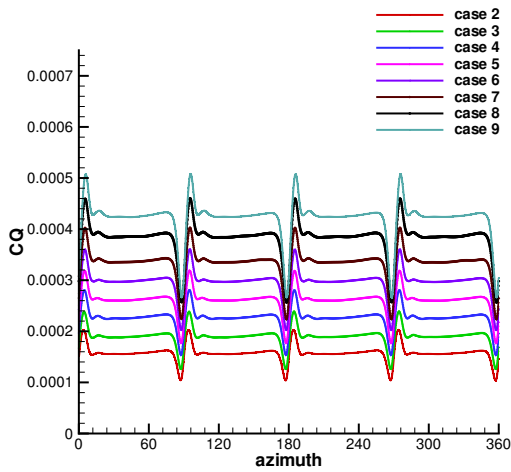
Figure 10: Temporal variation of C_T and C_Q of the top and bottom rotors in the last revolution for the coaxial system (case 7), after subtracting the values from the zero collective case.



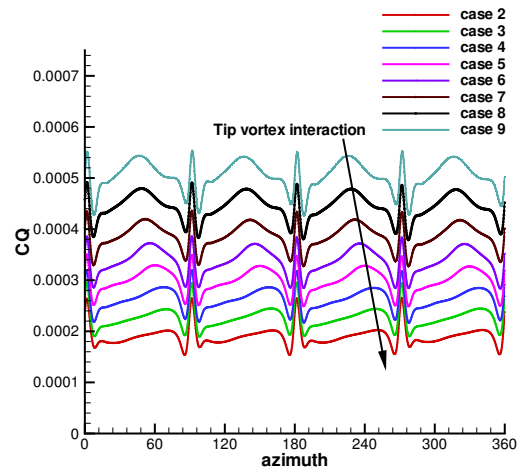
(a) Top rotor C_T variation



(b) Bottom rotor C_T variation

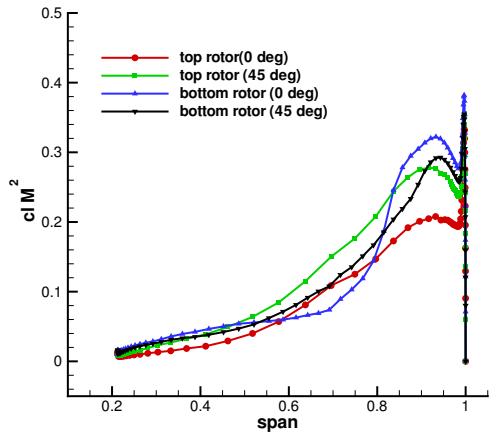


(c) Top rotor C_Q variation

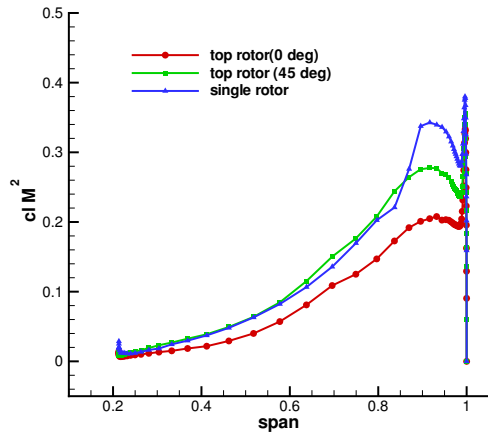


(d) Bottom rotor C_Q variation

Figure 11: Temporal variation of C_T and C_Q of the top and bottom rotors in the last revolution for all cases for the coaxial system.

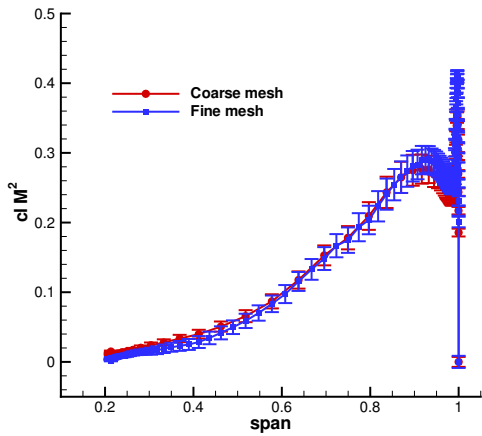


(a) Top and Bottom rotor

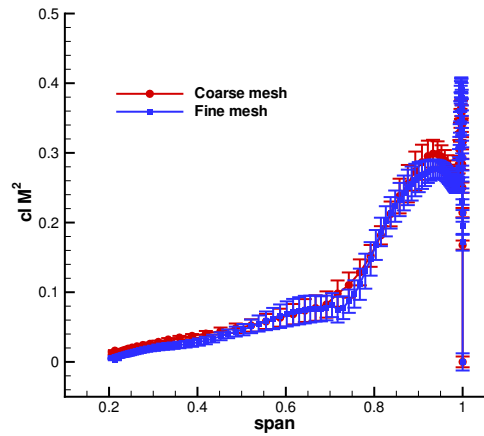


(b) Top rotor and Single rotor

Figure 12: Spanwise lift distribution at two different azimuth locations for the coaxial system (case 7).



(a) Top rotor



(b) Bottom rotor

Figure 13: Average lift distribution along with the RMS value of the fluctuation for the coaxial system (case 7).

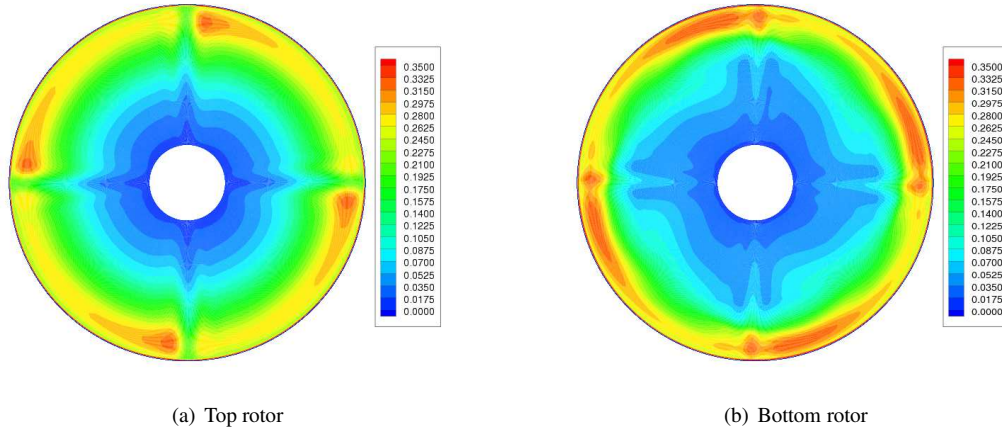


Figure 14: Sectional lift (cIM^2) contour for the coaxial system (case 7).

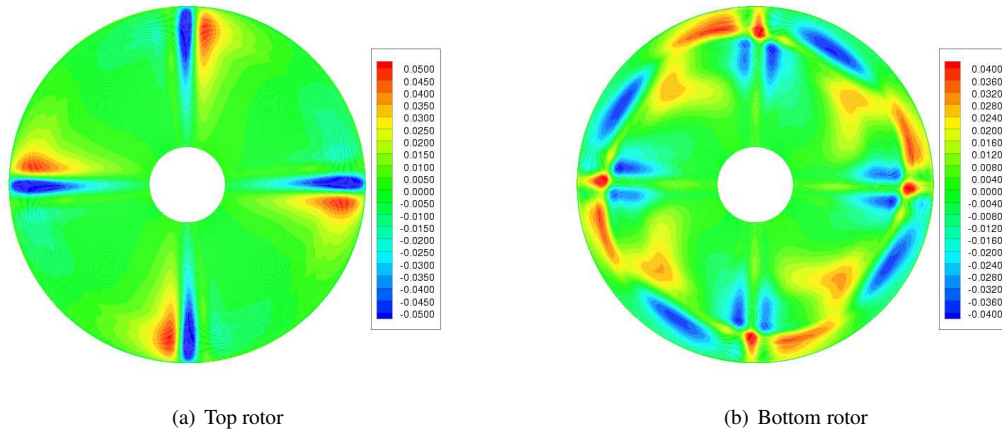
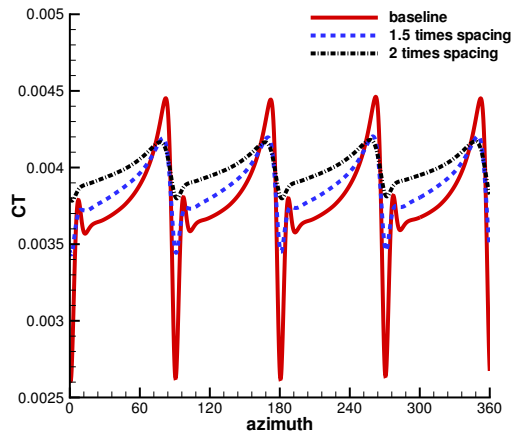
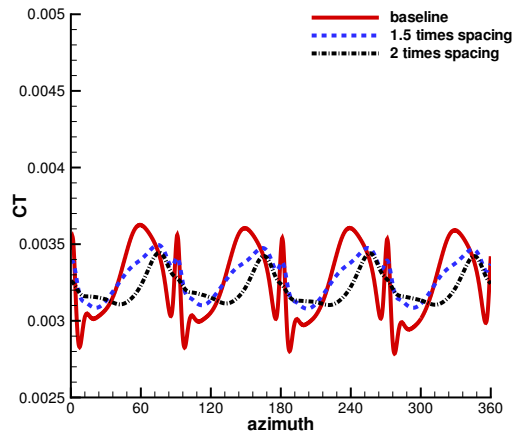


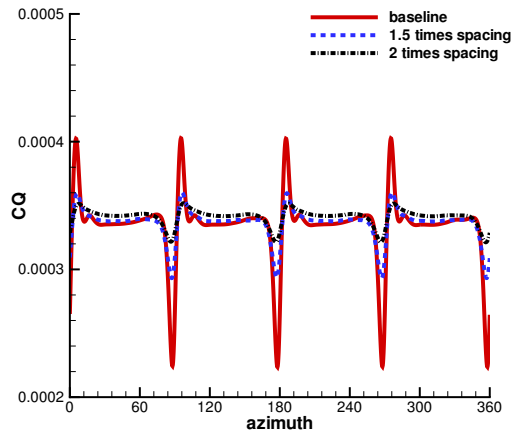
Figure 15: Fluctuation in sectional lift (cIM^2) contour for the coaxial system (case 7).



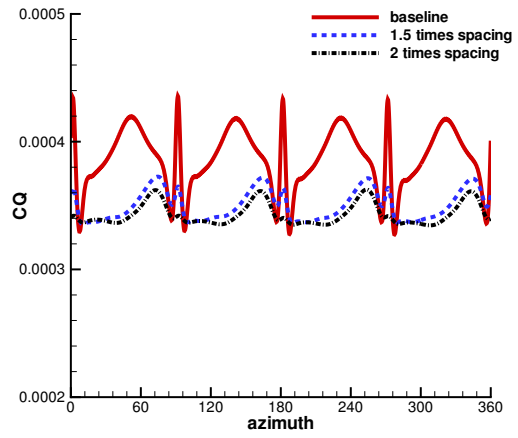
(a) Top rotor thrust



(b) Bottom rotor thrust

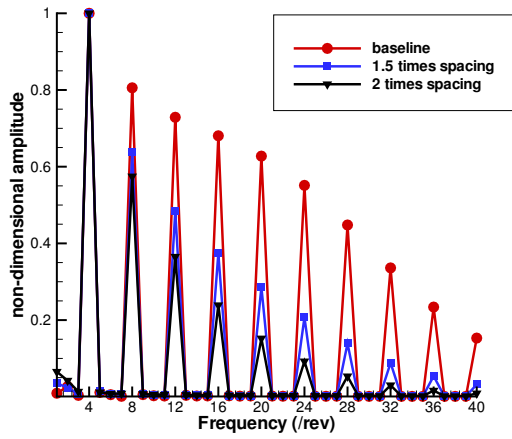


(c) Top rotor power

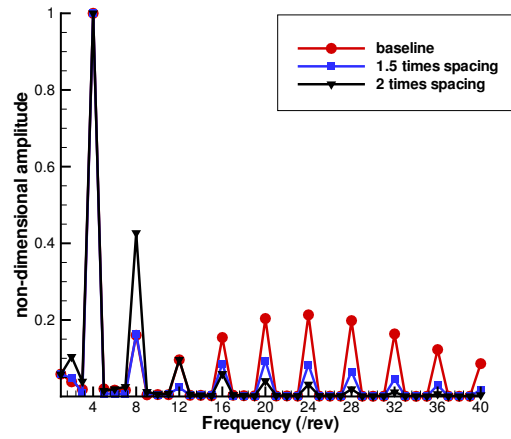


(d) Bottom rotor power

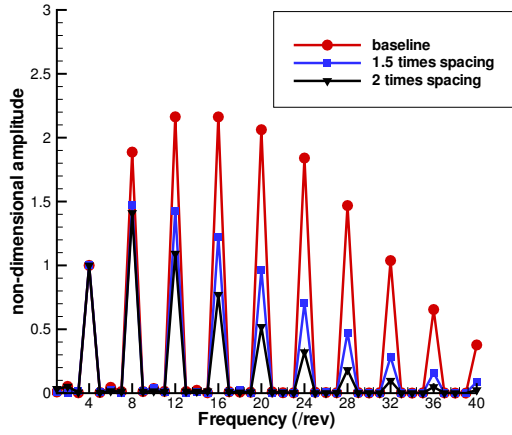
Figure 16: Effect of rotor spacing on the forces for the coaxial system (case 7).



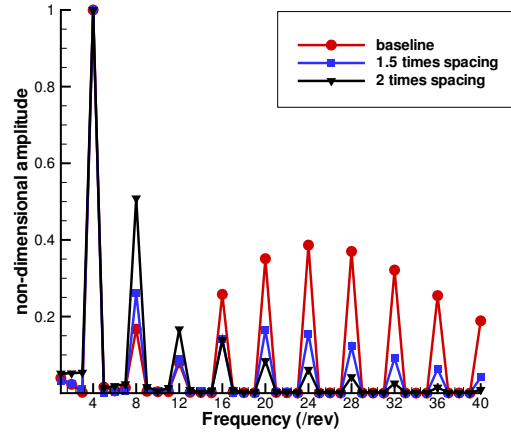
(a) Top rotor thrust



(b) Bottom rotor thrust

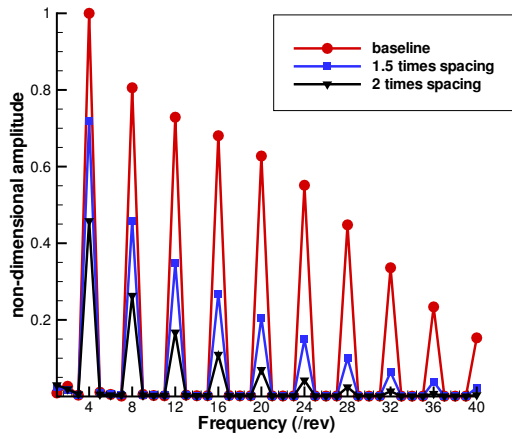


(c) Top rotor power

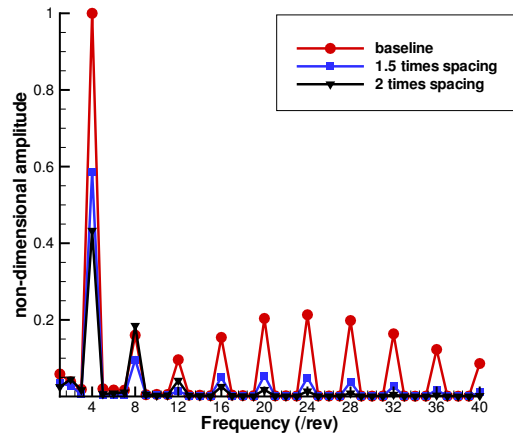


(d) Bottom rotor power

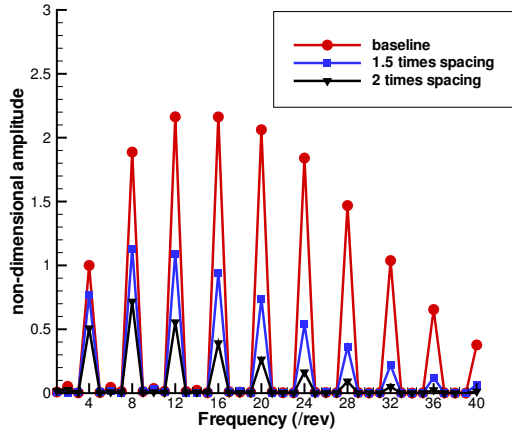
Figure 17: Effect of rotor spacing on the frequency distribution, normalized by the amplitude of 4/rev frequency, for the coaxial system (case 7).



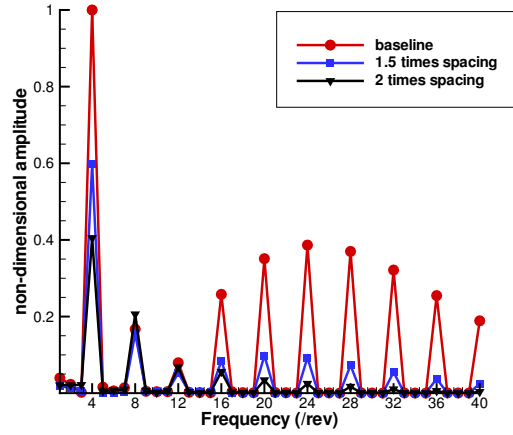
(a) Top rotor thrust



(b) Bottom rotor thrust



(c) Top rotor power



(d) Bottom rotor power

Figure 18: Effect of rotor spacing on the frequency distribution, normalized by the amplitude of 4/rev frequency of the baseline case, for the coaxial system (case 7).

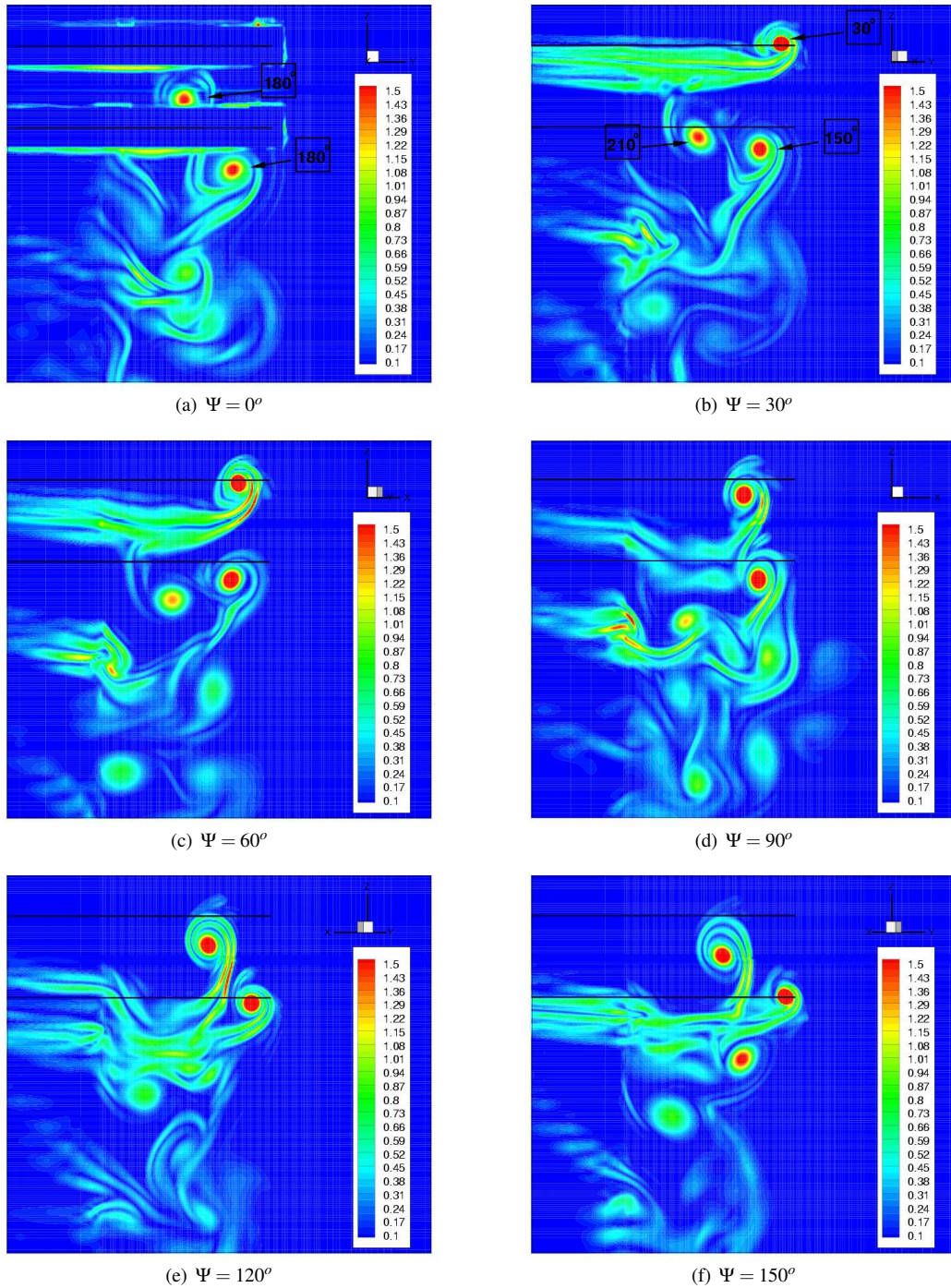
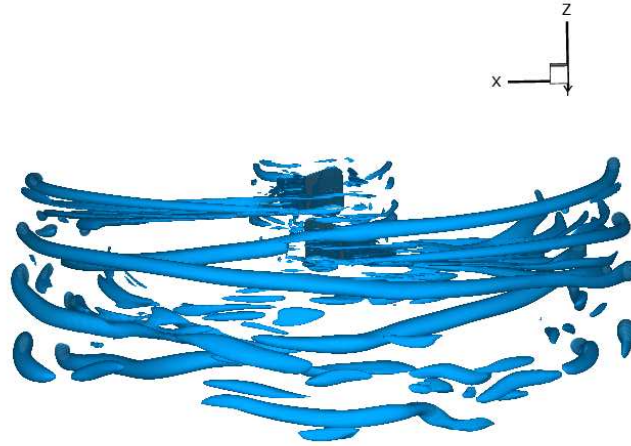
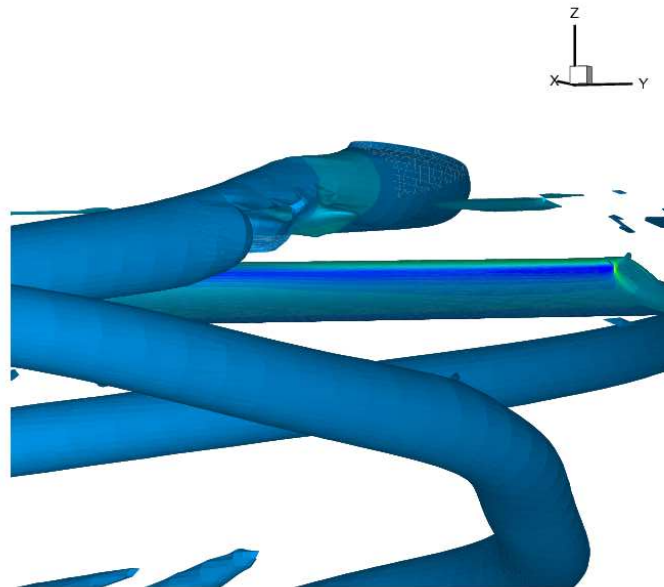


Figure 19: Vorticity magnitude contours at various azimuth locations in space for the coaxial system at an instant when blades are aligned (case 7).



(a) Vortex structures



(b) Tip vortex from top rotor interacting with bottom rotor

Figure 20: Iso-surfaces of the second invariant of vorticity magnitude ($q = 0.1$) for the coaxial system (case 7).